Investigation of orientation gradients around a hard Laves particle in a warm-rolled Fe₃Al-based alloy using a 3D EBSD-FIB technique

J. Konrad, S. Zaefferer, D. Raabe *

Max-Planck-Institut für Eisenforschung, Abteilung Mikrostrukturphysik und Umformtechnik, Max-Planck-Str. 1, 40237 Düsseldorf, Germany

Abstract

We present a study of the microstructure around a hard Laves particle in a warm-rolled intermetallic Fe₃Al-based alloy. The experiments are conducted using a system for three-dimensional orientation microscopy (3D electron backscattering diffraction, EBSD). The approach is realized by a combination of a focused ion beam (FIB) unit for serial sectioning with high-resolution field emission scanning electron microscopy with EBSD. We observe the formation of steep 3D orientation gradients in the Fe₃Al matrix around the rigid precipitate which entail in part particle-stimulated nucleation events in the immediate vicinity of the particle. The orientation gradients assume a characteristic pattern around the particle in the transverse plane while revealing an elongated tubular morphology in the rolling direction. However, they do not reveal a characteristic common rotation axis. Recovered areas in the matrix appear both in the transverse and rolling directions around the particle. The work demonstrates that the new 3D EBSD-FIB technique provides a new level of microstructure information that cannot be achieved by conventional 2D-EBSD analysis.
© 2005 Acta Materialia Inc. Published by Elsevier Ltd. All rights reserved.

Keywords: EBSD; Lattice rotation; Orientation gradient; Iron–aluminium; Texture

1. Introduction

1.1. Motivation for the introduction of a three-dimensional electron backscattering diffraction with a focused ion beam (3D EBSD-FIB) technique

EBSD is a well-established tool for the joint analysis of microtexture and phase distribution [1–6]. The ability to study the morphology (scanning electron microscopy, SEM), the crystallographic texture and the relationships of multiple polycrystalline phases (EBSD) as well as the chemical composition (energy dispersive X-ray analysis, EDX) simultaneously and at high lateral resolution renders modern SEM analysis a powerful tool for advanced microstructure characterization. Current high-speed systems are capable of measuring up to 80 EBSD frames per second

with a lateral resolution, depending on the material investigated, of 30–100 nm when using field emission gun SEM.

The possibilities of orientation microscopy via EBSD may now be dramatically enhanced by using a joint high-resolution field emission SEM-EBSD set-up in conjunction with a FIB system in the form of a 3D crystal orientation microscope [6,7]. With this technique successive sets of thin slices of material (minimum thickness ~50 nm) can be removed by sputtering with a high-energy ion beam operating at grazing incidence. Orientation microscopy of the flat surfaces so formed can be conducted by EBSD and EDX. The analysis results obtained for each serial section of the material are then used to reconstruct the original microstructure in three dimensions, including all features that can be jointly detected via EBSD and/or EDX mapping [6–8].

It is obvious that 3D analysis methods are essential in microstructure research. Two different approaches can be used for tomographic investigations. One consists of probing samples by transmitting radiation through them, such

---

as X-rays, electrons or neutrons. From the projections obtained the 3D microstructure can be reconstructed [9–13]. These techniques have the main advantage of being non-destructive, thus allowing the study of time-dependent processes. However, such tomographic transmission techniques may be either limited by the amount of information they provide, particularly for crystalline materials, or they become quite time consuming. Furthermore, the spatial resolution of X-ray-based techniques is currently limited to the range of 1–2 μm in all dimensions.

The second approach to tomography is serial sectioning and subsequent reconstruction of objects by stacking information obtained in subsequent slices of material. The past 40 years have seen a dramatic evolution in the development of such techniques. In 1962 Hillert et al. [14] produced moving images of successive serial sections in order to show the true 3D structure of an entire pearlite colony. Eichen et al. [15] studied the growth of Widmanstätten ferrite by measuring the change in the length of plates with increasing depth through serial sections. Hopkins and Kraft [16] used a cinephotomicrographic recording of the microstructure of a specimen undergoing controlled electrolytic dissolution. Their results were subsequently represented by building a 3D physical model of plexiglas to show the eutectic fault structure in a Cu–Al alloy. Hawbolt and Brown [17] used serial sectioning to study the shapes of grain boundary precipitates in an Ag–Al alloy. Barrett and Yust [18] visualized the 3D interconnectivity of voids in a sintered Cu powder.

The application of *automated* preparation and image acquisition was used for serial sectioning approaches by Li et al. [19], Kral et al. [20] and Hung et al. [21]. The work by Li et al. [19] deals with the 3D characterization of reinforcing Si particles in an Al matrix. In the study by Kral et al. [20] proeutectoid cementite, proeutectoid ferrite and an entire pearlite colony were characterized using a computer-aided visualization of 3D reconstructions from images obtained by serial sectioning. The work by Hung et al. [21] reflects recent improvements in the investigation of proeutectoid cementite precipitates at an early stage of growth.

The direct use of the FIB technique for sample surface preparation – independent of its application in conjunction with EBSD – is nowadays a well-established experimental approach (e.g. [22,23]). For instance, the use of FIBs as a tool for targeted preparation of transmission electron microscopy (TEM) foils with precise lateral resolution is nowadays well established [24]. Well-targeted ex situ preparations of series of sections for EBSD analysis with SEM [25] or isolated surfaces for EBSD investigations [26] have recently also been successfully performed. Also, the technique of serial sectioning with a FIB has been used for a 3D Auger microanalysis technique [27].

Our current approach for a full in situ 3D EBSD-FIB method was inspired by the first 3D EBSD analysis which was performed and reported by Uchic and Groeber [7,28,29]. The combination of EBSD-based orientation microscopy with serial sectioning via a FIB microscope has a number of important advantages over the previously mentioned sectioning techniques: FIB sectioning allows the highly controlled removal of thin layers of material with a minimum slice thickness of approximately 50 nm; also, serial sectioning can be performed in a fully automated fashion which allows one to investigate relatively large regions of up to 50 μm × 50 μm × 50 μm. The combination of these advantages with automated high-resolution orientation microscopy is possible, since the EBSD method offers an immensely rich spectrum of crystallographic information on the portion of the probed material, which exceeds the information obtained from most other microscopy techniques (except, in some cases, for orientation microscopy via TEM). This information includes, for example, the precise shape of grains, position and crystallographic character of interfaces, defect densities in grains and texture evolution at very small scales. All these can be measured at a lateral resolution of approximately 50 nm and less depending on the material under investigation.

1.2. Justification for the application of a 3D EBSD method to particle-containing Fe_3Al-based alloys

1.2.1. Introduction to Fe_3Al-based alloys

Fe_3Al-based alloys have long been investigated owing to their excellent oxidation and sulfidation resistance [30]. The low room temperature ductility (<5%) and sharp drop in strength above 600 °C have limited their use as structural materials [30]. Control of microstructure and texture evolution combined with strengthening by second-phase particles and intrinsic ductilization by alloying with chromium [31] mark the current strategies for rendering Fe_3Al-based alloys into useful engineering materials. Our present investigation is concerned with this context, placing particular attention on the effect of hard second-phase particles on the microstructure evolution. This classic problem of physical metallurgy is an obvious and ideal topic for the application of the novel 3D EBSD technique.

1.2.2. Texture break-up and microstructure stabilization

Texture evolution of Fe_3Al-based alloys during hot and warm rolling is characterized by two very stable typical body-centered cubic (bcc) texture components, namely the α- and the γ-fiber (⟨110⟩∥RD and ⟨111⟩∥ND (RD, rolling direction; TD, transverse direction)) [32–36]. Additionally, large grains of the 45° normal direction (ND) rotated cube texture component ({001}⟨110⟩) are typically present after rolling and even after the final heat treatment [37,38]. It is well known from earlier investigations [39–41] that this texture component deforms very homogeneously during rolling of bcc, B2 and DO_3 structured materials and thus shows a sluggish recrystallization behavior. Consequently, Fe_3Al-based alloys also tend to preserve their large grain size and the preferred 45° ND rotated cube texture component

during the hot-rolling process. In contrast to many steels where the face-centered cubic–bcc phase transition is exploited for breaking up the texture during processing, in Fe$_3$Al alloys the absence of this phase transformation requires the use of a different mechanism for controlling the texture in terms of a discontinuous break-up.

One strategy to solve this problem consists of inserting second-phase particles. The presence of sufficiently large particles in the matrix can entail an additional recrystallization nucleation mechanism, namely particle-stimulated nucleation (PSN) [42–46], which can promote a more homogeneous and refined grain size distribution. In a previous investigation it was indeed observed that the texture of a particle-containing Fe$_3$Al alloy showed a modest change in hot-rolling, warm-rolling and recrystallization textures compared to particle-free Fe$_3$Al alloys [36]. However, in either case (with and without particles) the main components of the observed rolling textures remained essentially unaffected, i.e. the texture mainly consisted of the α- and γ-fibers. This means that the influence of the particles on the recrystallization behavior does not entail a severe weakening or even randomization of the crystallographic texture upon heat treatment.

Another important observation about the effect of PSN on the microstructure of Fe$_3$Al alloys was made by McKamey and Pierce [47]. They reported that the best room temperature tensile strength and ductility were attained in specimens that had been heat treated to relieve internal stresses which were induced by the preceding fabrication process. In contrast to common metallurgical intuition they found that the best properties were achieved in those samples that had a *minimum* number of recrystallized grains. They hence concluded that the occurrence of PSN would degrade rather than improve the material properties of Fe$_3$Al alloys.

Owing to this ambivalence of the role of particles and the PSN effect in Fe$_3$Al alloys we have in this work chosen as a central problem the investigation of the formation of orientation gradients in the vicinity of large particles in Fe$_3$Al during plastic deformation using the new 3D EBSD technique outlined above.

1.2.3. The role of orientation gradients at particles in rolled Fe$_3$Al-based alloys

Particles create strong orientation gradients due to the activation of different slip systems and their mutual interaction. Recovery in areas with steep orientation gradients may lead to the rapid formation of large-angle grain boundaries [42]. A sufficient gradient to create these conditions is of the order of 15°/μm [48]. The formation of new grains, therefore, starts preferably in regions with the steepest orientation gradients and the largest local driving forces. Additionally, at the particle interface of a prospective nucleation site one surface does not have to be created (heterogeneous nucleation). The matrix nucleation events are, therefore, to be expected at the particle–matrix interface.

Local crystallographic orientation gradients can be described by defining a rotation axis together with start and end orientations. In the present work the reference orientation for the quantification of an orientation gradient is referred to as matrix orientation. This corresponds to the orientation of the matrix crystal outside of the inhomogeneous deformation zone around the particle. The end orientation is the orientation next to the particle interface. In cases where recrystallization had started it is referred to as the nucleus orientation. The start and end orientations of the gradients define the possible orientation spectrum from which newly recrystallized grains emerge and recruit their respective orientation.

2. Experimental

2.1. Sample preparation

An alloy with a composition of Fe–26% Al–5% Cr–0.2% Zr–0.05%C (in at.%) was produced in an induction furnace under an argon atmosphere and cast into a copper mold. The subsequent heat treatment was conducted at 1200 °C in air for 4 h followed by air cooling. The goal of the annealing treatment was to increase the average size of the Laves-phase ((Fe,Al)$_2$Zr) precipitates which occur as an interdendritic eutectic lamellar phase within the Fe$_3$Al matrix [49]. The heat treatment resulted in mainly spheroidized precipitates (Fig. 1). The average diameter of the precipitates increased from 1.4 to 4.4 μm. The large precipitate size was chosen for obtaining pronounced orientation gradients around the precipitates during deformation [42,43].

Warm rolling (20 passes) of the initially hot-rolled and recrystallized material was performed at 630 °C resulting in a sheet of 1 mm thickness (true logarithmic strain: 1.7; engineering thickness reduction: 82%). The large thickness
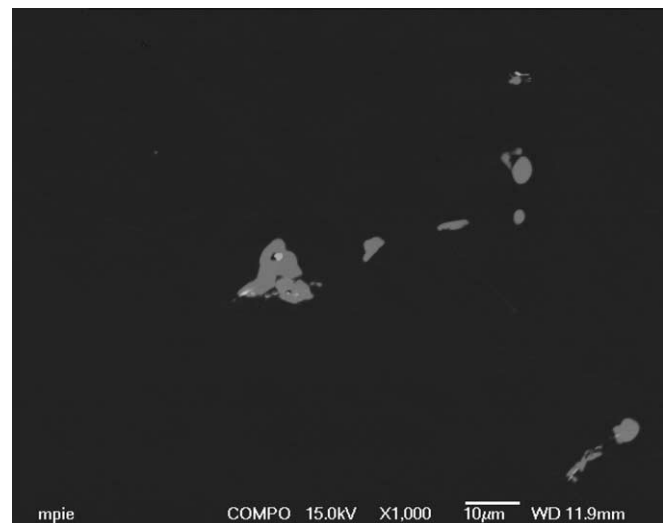

Fig. 1. SEM micrograph of the investigated alloy after the 4 h heat treatment at 1200 °C.

reduction was imposed to generate a heavily deformed non-recrystallized microstructure with a large amount of stored elastic energy [50].

2.2. Set-up of the FIB-SEM experiment for 3D EBSD analysis

Small samples ($10 \times 5 \times 1$ mm^3) were cut from the rolled sheet by spark erosion. The geometry for FIB-SEM requires that the sampling area is positioned close to a sample edge. Therefore, in order to observe features in the center of the sheet, where a deformation state close to plane strain is expected, the sample was ground to approximately half of its original thickness and the ND/TD plane of the sheet close to the center edge of the sample was inspected.

A Zeiss XB1560 crossbeam instrument was used, with a field emission electron column and a Ga$^+$ ion emitter. It was equipped with secondary electron, backscattered electron and scanning transmission electron detectors. For orientation microscopy an EBSD detector (TSL/EDAX, DigiView 1612 camera) was installed at a position opposite the FIB column (Fig. 2). This position allows for the quick and precise change between FIB milling for serial sectioning (sample at 36°) and EBSD mapping (sample at 70°). Additionally, an EDX detector was mounted for the determination of the material composition. A gas injection system enabled the deposition of various coatings (W, Pt, SiO$_2$) from organic precursor gases for surface protection. The spatial resolution of 3D pixels for EBSD analysis may reach about $50 \times 50 \times 50$ nm^3.

An area of interest, i.e. a large particle (Laves phase) including its Fe$_3$Al matrix environment, was selected using backscattered electron images on a slightly polished surface (Fig. 3). These images provided sufficient composition and
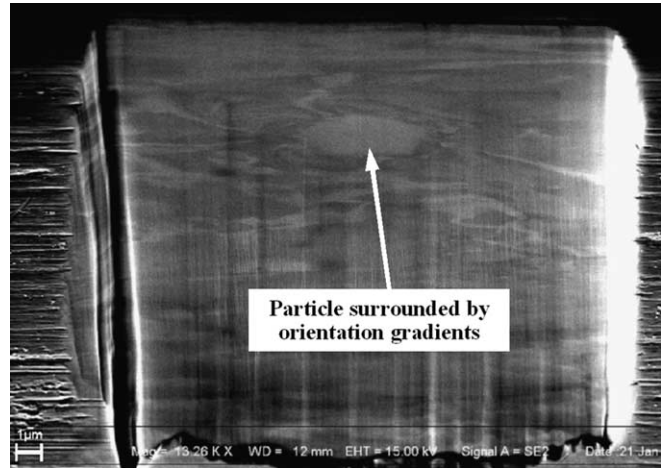

Fig. 3. SEM image (SE) of the sampling area after the first FIB preparation.

orientation contrast and allowed for the identification of a large Laves-phase particle surrounded by pronounced orientation gradients.

2.3. 3D orientation microscopy

For the serial sectioning procedure the FIB was operated at an accelerating voltage of 30 kV and a milling current of 500 pA (the instrument allows beam currents from 10 pA to 50 nA) [51]. The volume milled between two successive sections amounted to 20 μm (TD) × 2 μm (RD) × 50 μm (ND, milling depth) (Fig. 4). Milling of one such volume portion required 40 min. It was conducted by scanning the ion beam 20 times across the trapezoid surface shape (Fig. 4). The trapezoid was positioned applying the
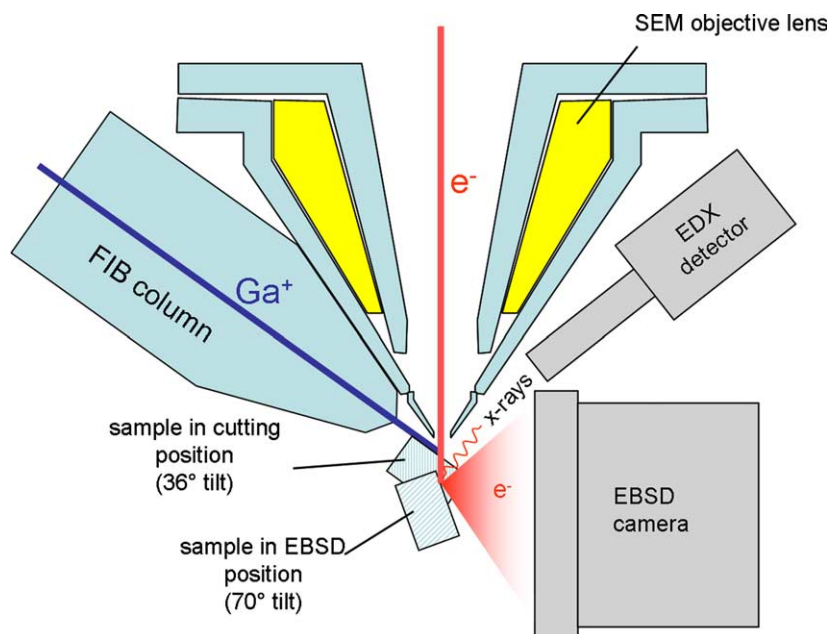

Fig. 2. Schematic representation of the experimental setup for the 3D EBSD-FIB method.
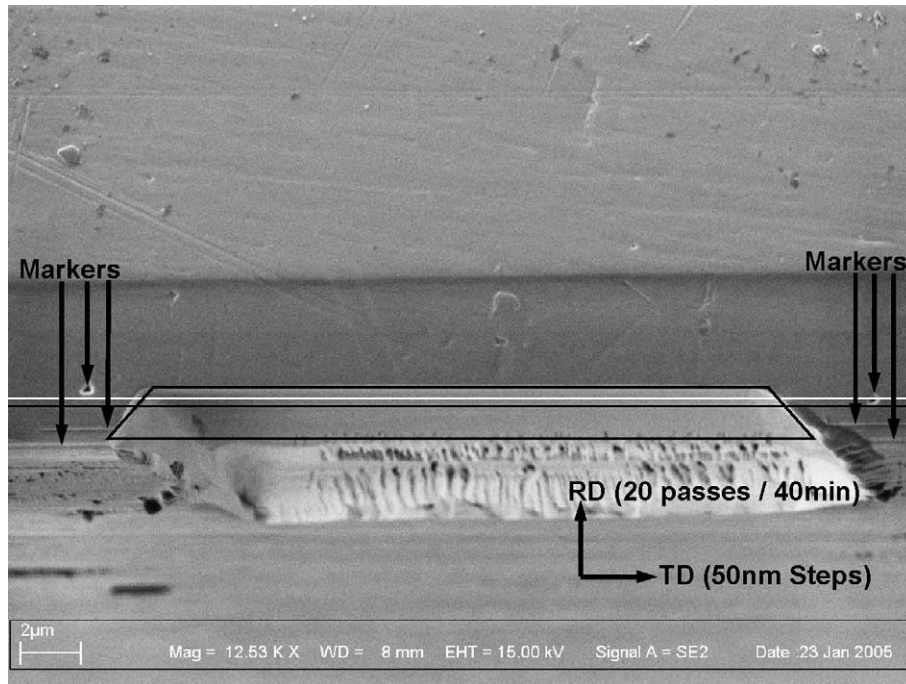
Fig. 4. FIB SE image of the milling area of the sixth slice indicating the markers and the scanning strategy.

FIB-induced secondary electron image. The section thickness was selected manually by a defined beam shift of 400 nm in the RD relative to the preceding milling step. The milled volume exceeded the required section thickness to avoid re-deposition of milled material at the sample edges which would entail shadowing of the EBSD detector and a reduction of the observation area. Milling and sample positioning together required about 1 h for each section. The exact thickness of each section was finally determined using image analysis software and markers for each frame that were placed by the FIB before the serial sectioning procedure. The markers consisted of six grooves milled parallel and perpendicular to the sample edge (Fig. 4). All markers were milled using a low beam current of 50 pA to obtain sharp grooves. The average accuracy of this z-scale definition was ±3.7%.

After each serial sectioning step the sample was tilted into the EBSD position and Kikuchi diffraction patterns were acquired using a 50 nm step size on an area of 20 μm × 46 μm. Each orientation map required a measurement time of about 3 h at a frame rate of 40/s. The measured orientation data were processed using OIM Analysis Version 4 software by TSL (EDAX). First, a classic 2D analysis was performed for each section including the reconstruction of maps for pattern quality, inverse pole figure coding and kernel average misorientation.

2.4. 3D visualization of the EBSD data

For the 3D rendering procedure of the experimental data we used the non-commercial software package IMOD [52]. For this purpose special types of EBSD data sets were exported for each section using the standard EBSD analysis software. For visualization of the orientation gradients reference orientations for each gradient zone were selected first. The 2D EBSD software was used to generate Boolean (black, white) bitmap images mapping 5° interval steps in all areas containing misorientations of up to 45°. One map was created and exported as a bitmap image for each misorientation interval (5°) in each gradient region for all sections. Using 8 sections × 4 gradient zones × 8 images (between 5° and 45°) amounts to 256 separate Boolean images in total. The grains with orientations belonging to different texture components as well as the areas of local misorientations below 2.5° were also exported as binary bitmap images for each section. The binary 2D images were combined into a stack of eight sections for each feature (gradient interval, texture component or local misorientation) and subsequently manually aligned in x, y and z directions. For the latter procedure small variations in the distances between the consecutive scans were taken into account. The IMOD software was then used to define the contours of the respective microstructure features under inspection for each section using appropriate threshold values. The contours were reproduced by a mesh consisting of points (nodes) connected by straight lines. These nodes of the different contours generate the model which combines all necessary spatial information and consists of the spatial coordinates of each point and its assignment to the respective object that it represents. The IMOD software package uses a triangulation approach to construct an enveloping surface using the nodal points from each section. Finally all surfaces generated can be displayed using standard 3D rendering techniques.

3. Results and discussion

3.1. FIB–surface interaction and influence on the EBSD analysis

Ion beam–surface interactions have been studied in detail by several groups [24,25,53–55]. The main issues associated with beam–surface interactions in the present context are, first, the problem of selective sputtering depending on the crystallographic direction and, second, the formation of a rough or even amorphous surface during serial sectioning. It was earlier reported that the slope angle of the trench wall is strongly influenced by the milling conditions [53]. This can lead to geometric errors due to a non-coplanar, distorted sectioning and to shadows on the phosphor screen required for EBSD pattern acquisition. Another aspect that strongly depends on the material under investigation as well as on the milling conditions is that implanted gallium ions can damage the sample surface and increase the defect density [54]. The worst possible scenario conceivable in this context is the generation of an amorphous layer in the surface under investigation [55]. If such an amorphous layer has a thickness of the order of the information depth of the EBSD method (5–15 nm depending on the material) a noticeable weakening or complete disappearance of the Kikuchi patterns will result.

In order to control these aspects we compared the EBSD image quality obtained from surfaces prepared using the FIB with that obtained from corresponding surfaces of mechanically prepared samples of the same material. The image quality (IQ) is the sum of the detected peaks in the Hough transform. Corresponding IQ values of highly deformed matrix regions range from 80 to 170 while recrystallized grains typically show IQ values up to 220. These values correspond to those measured for a similar, *mechanically* polished sample. For the precipitate that, based on former investigations of this material by EBSD and EDX [50], was identified as the C14 Laves-phase $(Fe,Al)_2Zr$ [49], however, no detectable Kikuchi pattern was observed. This indicates that surface amorphization of the Laves phase reaches deeper than approximately 10 nm, which is the information depth of the EBSD method. Within the Fe_3Al matrix the damage layer seems not to be thicker than a few nanometers so that EBSD could be applied without any problems and at high acquisition rates on surfaces pre-

pared using the FIB. Other authors reported a sidewall amorphization depth of 20 nm on Si [55] after milling with 30 keV ions. The authors of that study suggested that the amorphization depth decreases linearly with the ion energy.

A different problem caused by FIB milling is the formation of vertical grooves in the milled surface, which is referred to as curtaining. This phenomenon usually occurs at the lower end of the milled surface. The reason for this phenomenon is the loss of focus at larger depths or too large a step size of the milling beam. Curtaining limits the area suited for EBSD analysis to a depth of approximately 50 μm below the edge. We observed that the curtaining phenomenon can be reduced by correct focusing, a small milling step size and the deposition of a protective layer (Pt, W) on the surface perpendicular to the beam direction prior to milling.

3.2. Microstructure and local texture

The $(Fe,Al)_2Zr$ Laves phase particle is located within a large grain with γ-fiber orientation ($\langle 111 \rangle \| ND$). Conventional 2D EBSD analysis of the sample shows four strong, spatially independent orientation gradient zones around the particle which had developed during warm rolling
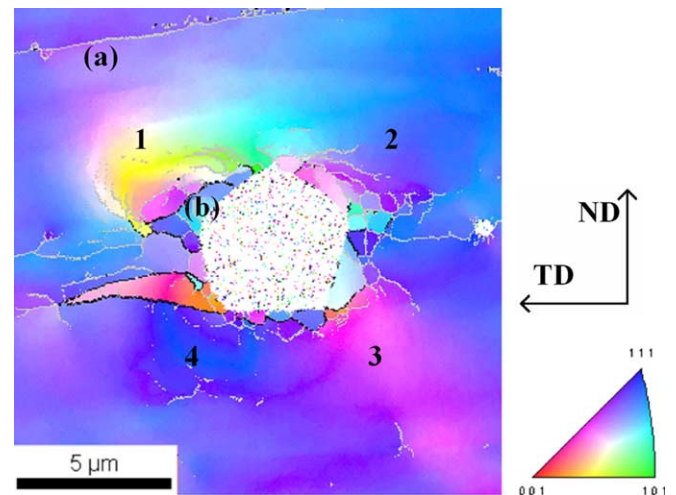

Fig. 5. Inverse pole figure map of the normal direction (ND) of the first section analyzed by the 3D EBSD-FIB method. (a,b) Mark the reference and the nucleus orientations, respectively, of gradient 1. The counters 1–4 indicate the four different analyzed gradient zones.

Table 1
Orientations of the matrix and of the four analyzed reference orientations (nuclei), their misorientation with respect to the surrounding matrix, and the average orientation gradients (ND: normal direction of rolled sheet; RD: rolling direction of rolled sheet)

Orientation	Plane ∥ to ND	Direction ∥ to RD	Total misorientation (°)	Gradient (°/μm)
Matrix orientation	$(\bar{1}1\bar{1})$	$\langle \bar{1}01 \rangle$	–	
Reference (nucleus) orientation 1	$(\bar{2}\bar{1}4)$	$\langle \bar{1}2\bar{1} \rangle$	44	18
Reference (nucleus) orientation 2	$(\bar{5}22\bar{2})$	$\langle 6\bar{1}4 \rangle$	36	12
Reference (nucleus) orientation 3	(652)	$\langle \bar{1}1\,\bar{1}0\bar{8} \rangle$	34	21
Reference (nucleus) orientation 4	$(\bar{1}31\,2\,\bar{2}0)$	$\langle \bar{2}00\,\bar{1}3 \rangle$	26	8

The values for the total misorientation are calculated as the orientation difference between each of the four reference (nucleus) orientations and the matrix orientation far away from the particle.
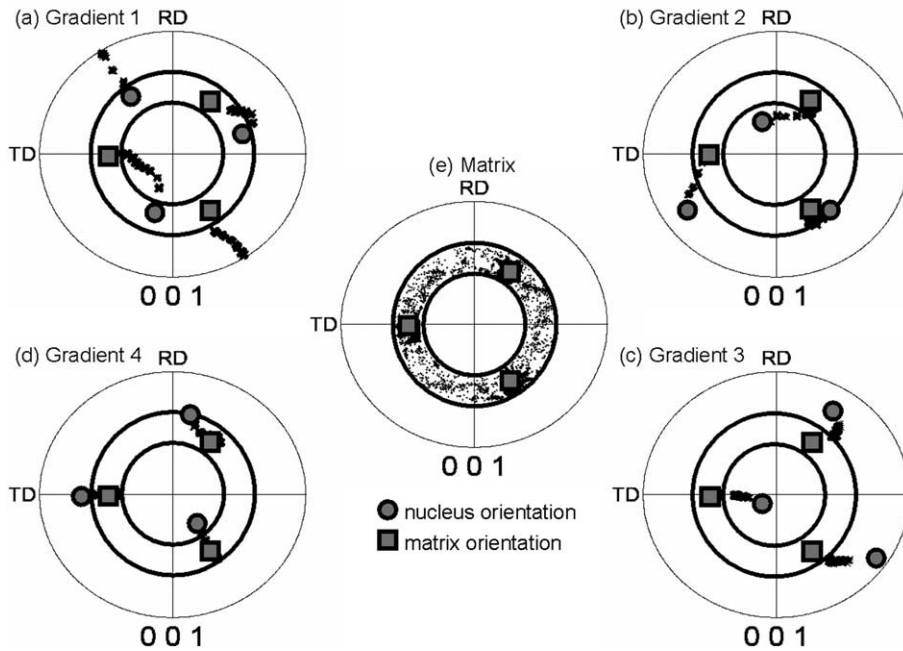
Fig. 6. Discrete pole figures of the four gradients (a–d) and the matrix orientation within the γ-fiber grain (e). Circles and squares refer to the start (nucleus) and end (matrix) orientations, respectively.

(Fig. 5). Table 1 shows for all four gradient regions their respective start and end orientations, the accumulated misorientations and the orientation gradients. In the immediate vicinity of the Laves particle, where the orientation gradients are steepest, several small, gradient-free grains and subgrains are found which were obviously formed by a recrystallization or recovery process, respectively. These zones are referred to as nucleus orientations in Table 1.

The orientation change along all orientation gradients is shown in the pole figures in Fig. 6. In the following, we discuss the most prominent one, namely gradient 1, in more detail. For this gradient the crystal lattice rotates from the orientation of the matrix crystal, which belongs to the γ-fiber, by more than 40° over a change of only approximately 6 μm. The largest portion of this enormous lattice rotation occurs in fact over a distance as small as 2 μm
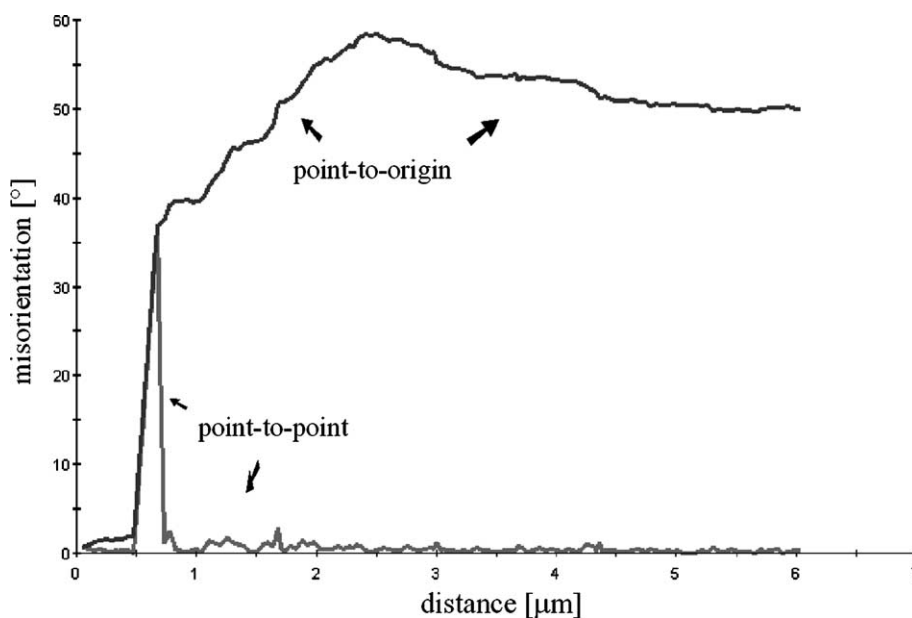

Fig. 7. Misorientation profile in gradient zone 1 (see details in Table 1), including the newly formed grain adjacent to the hard Laves particle. The curve "point-to-point" indicates the profile of the orientation changes between abutting points. The curve "point-to-origin" refers to a profile of the orientation changes between all points and a reference point (see details for the selection of the reference orientations in Section 2 and in Table 1).
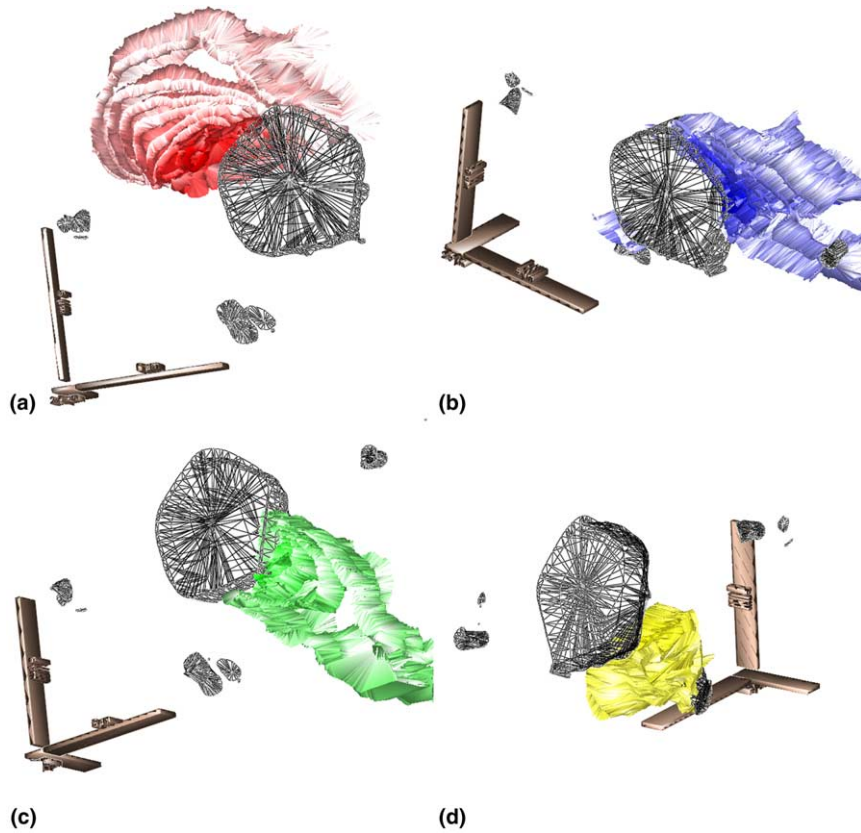
Fig. 8. 3D visualization of the four orientation gradient zones in the Fe$_3$Al matrix around the hard Laves-phase particle. The images were generated using the IMOD software package [52]. A characteristic color code is used for each separate gradient zone: (a) gradient 1; (b) gradient 2; (c) gradient 3; (d) gradient 4. Each shell indicated by the color gradient represents a misorientation interval of 5° relative to its respective reference orientation (Table 1). The micronbars represent 5 μm in ND and TD and 2.5 μm in RD.
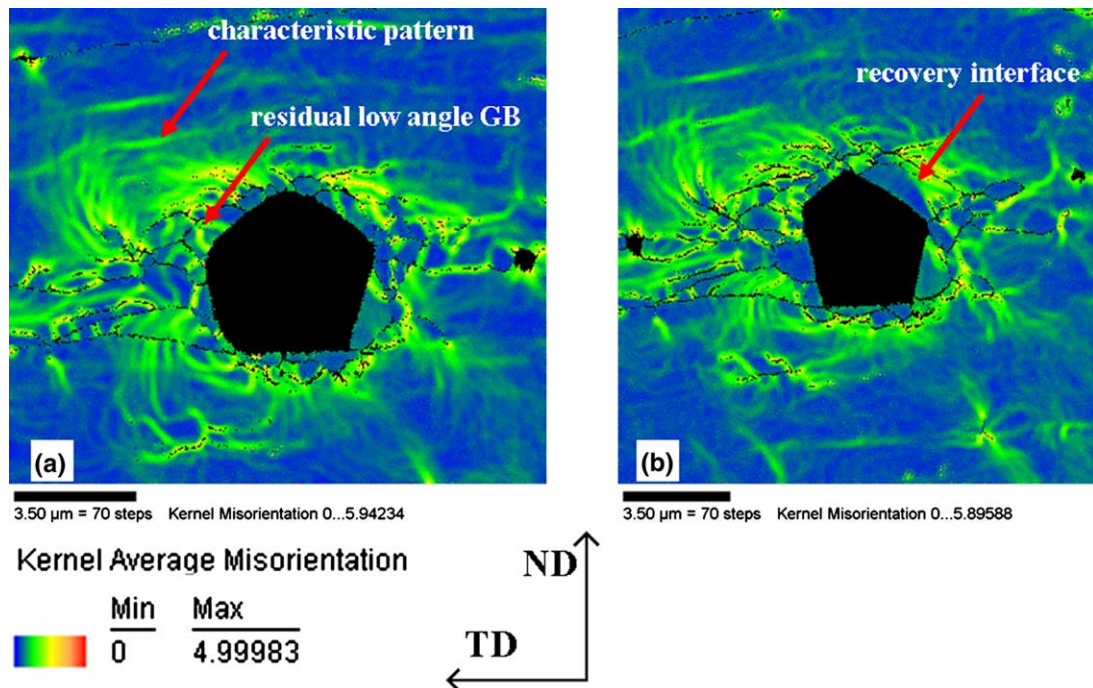

Fig. 9. maps of the Kernel average misorientation of two sections. Section (a) is the first cut. Section (b) is the fourth cut taken at a distance from the first one of 1.1 μm along RD.

close to the precipitate. Following the orientation path further in the pole figure leads one to the orientation of the small recrystallized grain immediately at the particle interface. Counting also this last reorientation step relative to the matrix orientation amounts at a total orientation distance of 60° between the matrix grain orientation and the new nucleus grain which was formed directly at the particle interface. The orientational and spatial proximity of the gradient and the newly recrystallized grain leads us to the assumption that this grain was formed by a recovery process in the area of the steepest part of the gradient. It may be estimated in this case that the initial gradient reached the very high value of almost 40°/µm in the immediate vicinity of the particle (Fig. 7). The end orientation of the gradient, i.e. the orientation of the newly formed grain, is – like the matrix orientation – positioned within the γ-fiber at a rotation of approximately 60° with respect to the start (reference) orientation. It is well known from
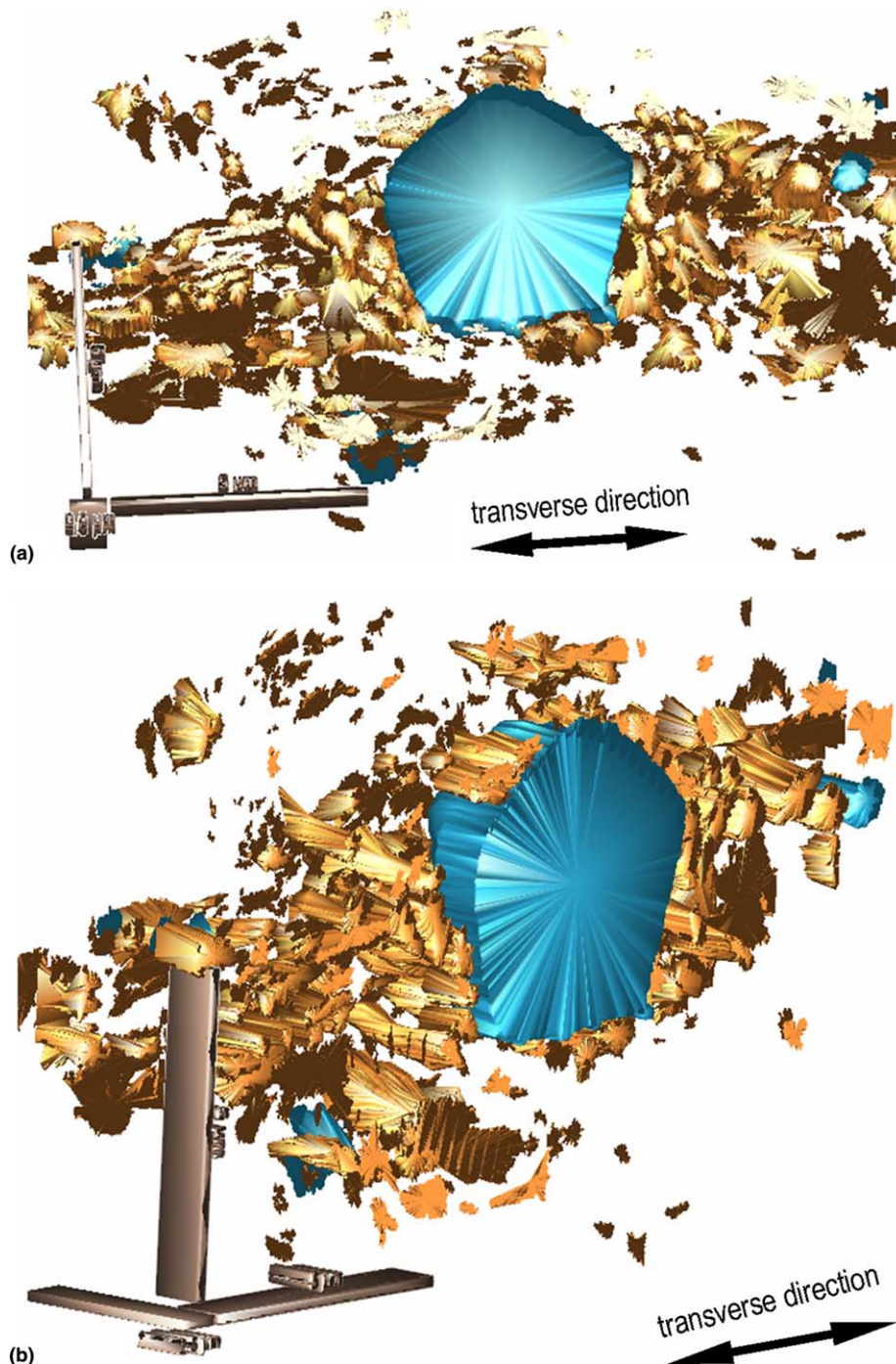

Fig. 10. 3D visualization of areas of low local misorientation in the vicinity of the Laves-phase particle. The Laves phase is colored blue. The areas which are characterized by a weak average local misorientation of less than 2.5° are colored gold.

the recrystallization of bcc steels [32,33,56–58], other bcc metals [32,40] and DO$_3$ structured materials [34,59] that recrystallization of new γ-fiber grains typically occurs inside originally γ-fiber oriented crystals at a rotation of 30° with respect to each other. In the present case, however, a comparison with the other gradient zones surrounding the particle, where the end orientations are somewhere outside of the γ-fiber, suggests that the situation of gradient 1 should not be regarded as a representative scenario for the nucleation of {1 1 1} oriented grains.

When comparing the orientation gradients along RD (which amounts to comparing the different sections) no additional rotation components could be identified. The 3D visualization supports this result by revealing a tube-like morphology of the gradients extended in RD instead of a spherical onion-type shell gradient arrangement (Fig. 8).

Deformed, recovered and recrystallized areas can be distinguished from each other by analyzing local or in-grain orientation gradients. For this purpose we use the kernel average misorientation maps of the gradient zones under inspection. These maps are constructed by calculating the kernel average misorientation of every measurement point up to its third nearest neighbors. Heavily deformed areas in the microstructure typically reveal high values of the local misorientation. The misorientation is, however, not neces-

sarily homogenously distributed but rather shows a characteristic pattern. This applies particularly in the vicinity of the Laves-phase particle (Fig. 9(a)).

Fully recovered areas appear in such mappings as zones that are essentially free of local misorientations. These areas are bounded by either low-angle grain boundaries or areas of higher local misorientation (Fig. 9(b)). Recrystallized grains are also free of local misorientations, but they are bounded by high-angle grain boundaries. As shown in Fig. 9(a), these recrystallized grains may also contain subgrains with recovered subgrain boundaries between them. Such zones are presumably retained during the recovery process in the grain interior. Fig. 10 provides a 3D presentation of these various recovered and partially recrystallized areas in the vicinity of the Laves particle. The 3D visualization colors the Laves phase in blue. The areas that are characterized by a weak average local misorientation of less than 2.5° are colored gold. It can be seen that large grains surround the particle in the ND/TD plane while a larger number of smaller grains or recovered zones can be found in a large volume spread out behind the particle along the RD and in a band-like zone around the particle in the ND/TD plane.

Fig. 11 shows the topography of the texture components which is obtained by assigning the measured 3D

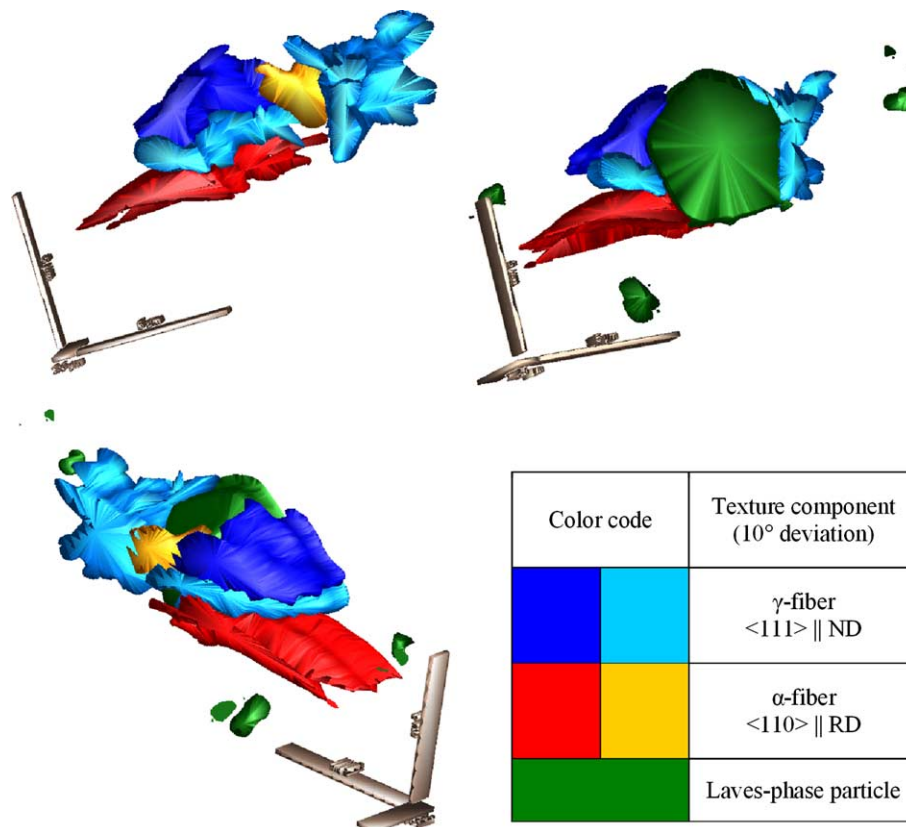| Color code		Texture component (10° deviation)
(blue)	(cyan)	γ-fiber <111> ‖ ND
(red)	(gold)	α-fiber <110> ‖ RD
(green)		Laves-phase particle

Fig. 11. 3D visualization of the topography of the main texture components surrounding the hard particle. This type of presentation is obtained by assigning the measured 3D EBSD orientations to specific crystallographic texture components which are typical of Fe$_3$Al alloys (γ-fiber, <111>‖ND; α-fiber, <110>‖RD). Both, the bright and the dark blue color coding are equivalently used to indicate affiliation to the γ-fiber. Red and orange are equivalently used to indicate affiliation to the α-fiber. Green color coding indicates the Laves particle.

EBSD orientations to specific crystallographic texture components typical of Fe$_3$Al alloys [37,38].

The visualization reveals that the dominant orientations surrounding the hard particle in the ND/TD plane belong to the γ-fiber. As shown in Fig. 9, these γ-fiber grains contain a substantial amount of recovered areas with surrounding large-angle grain boundaries. The formation of new grains which may assume the role of recrystallization nuclei therefore seems to occur preferably in the region close to the particle–matrix interface.

Behind the particle (when viewed along the RD), potential nucleation sites with a wider spread of orientations were found. This observation suggests that there is only a weak systematic crystallographic effect of the particle on the resulting topology and direction of the generated orientation gradients in the matrix.

To be more specific, we confirm that the PSN mechanism entails two types of effects. The first is a refinement of the grain size because the number of potential or genuine recrystallization nuclei is increased in the vicinity of those hard particles that fulfill the size criteria discussed by Humphreys and Ferry [42–45].

The second effect is the modification of the crystallographic texture. This change mainly consists of weakening the texture around particles compared to other nucleation mechanisms that work without particles. This does not necessarily imply that particle-affected textures are generally more randomized as opposed to those observed without the presence of nucleation at particles. The reason for this is that the texture components of the rolled state can be retained to a certain extent around particles and that not only random but also systematic orientation changes (typically weak TD rotations) are conceivable in the immediate vicinity of particles. It is plausible that the efficiency of the texture randomization around particles is influenced by their size and shape, their mechanical properties compared to those of the matrix, and by the preceding deformation process, i.e. by the stress–strain history imposed.

4. Conclusions

3D orientation microscopy has been applied to the study of PSN at a large, undeformable particle in a hot-rolled Fe$_3$Al-based alloy. The 3D investigations were carried out on serial sections created in a well-defined manner with a FIB in a Zeiss crossbeam FIB-SEM instrument. Each section was investigated by conventional 2D EBSD-based orientation microscopy with the same instrument. Subsequently the 2D orientation maps were merged to render the 3D microstructure of the sample portion inspected. The main conclusions are:

1. Serial sectioning using a FIB turned out to be highly efficient in preparing surfaces of up to 50×50 μm^2 which can be probed by EBSD (in the current study the probed volume amounted to 20 μm (TD) $\times$ 2 μm (RD) $\times$ 50 μm (ND, milling depth)). Serial sectioning and orientation microscopy required altogether about 4 h for each slice. The Laves-phase particle was damaged by the FIB beam so that no EBSD diffraction patterns were obtained for it.

2. The matrix material showed strong orientation gradients close to the hard particle. In the TD/ND plane the gradients amounted to approximately 40°/μm while they were much flatter along the RD. This means that the planes of equal misorientations form relatively long tubes along the RD.

3. In the area of the steepest gradients newly formed crystals were observed which were most likely formed by subgrain growth and coalescence. The 3D micrographs showed that the recovered (or recrystallized) areas are all distributed in an area of approximately 5 μm along the TD on either side of the particle while there are only few recovered areas behind the particle (when observed along the RD).

References

[1] Krieger Lassen NC, Juul Jensen D, Conradsen K. Scanning Microsc 1992;6:115–21.
[2] Adams BL, Wright SI, Kunze K. Metall Trans A 1993;24:819–31.
[3] Schwarzer RA. Micron 1997;28:249–65.
[4] Schwartz AJ, Kumar M, Adams BL, editors. Electron backscatter diffraction in material science. New York (NY): Kluwer Academic/Plenum Press; 2000.
[5] Humphreys FJ. J Mater Sci 2001;36:3833–54.
[6] Zaefferer S. Mater Sci Forum 2005;495–497:3–12.
[7] Groeber M, Haley B, Uchic M, Ghosh S. In: Ghosh S, Castro J, Lee JK, editors. Materials processing and design: modeling, simulation and application. Proc NUMIFORM 2004 (AIP Conference Proceedings). Melville, NY, USA: AIP Publishers; 2004. p. 1712–8.
[8] Dingley DJ, Randle V. J Mater Sci 1992;27:4545.
[9] Nielsen SF, Lauridsen EM, Juul Jensen D, Poulsen HF. Mater Sci Eng A 2001;319–321:179–81.
[10] Poulsen HF, Fu X, Knudsen E, Lauridsen EM, Margulies L, Schmidt S. Mater Sci Forum 2004;467–470:1363–72.
[11] Yang W, Larson BC, Pharr GM, Ice GE, Swadener JG, Budai JD, et al. Mater Res Soc Symp Proc 2003;750:Y.8.26.1.
[12] Larson BC, Yang W, Ice GE, Swadener JG, Budai JD, Tischler JZ. Nature 2002;415:887.
[13] Yang W, Larson BC, Pharr GM, Ice GE, Swadener JG, Budai JD, et al. Mater Res Soc Symp Proc 2003;779:W.5.34.1.
[14] Hillert M. In: Zackay VF, Aaronson HI, editors. The decomposition of austenite by diffusional processes. New York (NY): Interscience; 1962. p. 197–237.
[15] Eichen E, Aaronson HI, Pound GM, Trivedi R. Acta Metall 1964;12:1298–301.
[16] Hopkins RH, Kraft RW. Trans AIME 1965;233:1526–32.
[17] Hawbolt EB, Brown LC. Trans AIME 1967;239:1916–24.

[18] Barrett LK, Yust CS. Prog Trans AIME 1967;239:1172–80.
[19] Li M, Ghosh S, Richmond O, Weiland H, Rouns TN. Mater Sci Eng A 1999;265:153–73.
[20] Kral MV, Mangan MA, Spanos G, Rosenberg RO. Mater Char 2000;45:17–23.
[21] Hung CY, Spanos G, Rosenberg RO, Kral MV. Acta Mater 2002;50:3781–8.
[22] Szot J, Hornsey R, Ohnishi T, Minagawa S. J Vac Sci Technol B 1992;10:575–9.
[23] Giannuzzi LA, Stevie FA. Micron 1999;30:197–204.
[24] Sheng TT, Goh GP, Tung CH, Wang LF. J Vac Sci Technol B 1997;15:610–3.
[25] Matteson TL, Schwarz SW, Houge EC, Kempshall BW, Giannuzzi LA. J Electron Mater 2002;31:33.
[26] Prasad SV, Michael JR, Christenson TR. Scr Mater 2003;48:255–60.
[27] Cheng Z, Sakamoto T, Takahashi M, Kuramoto Y, Owari M, Nihei Y. J Vac Sci Technol B 1998;16:2473–8.
[28] Uchic MD, Groeber M, Wheeler IV R, Scheltens F, Dimiduk DM. Microsc Microanal 2004;10:1136–7.
[29] Uchic MD, private communication at the Freiburg III conference, Freiburg, Germany; May 2005.
[30] McKamey CG, DeVan JH, Tortorelli PF, Sikka VK. J Mater Res 1991;6:1779.
[31] Huang YD, Yang WY, Sun ZQ. Intermetallics 2001;9:119.
[32] Hölscher M, Raabe D, Lücke K. Steel Res 1991;62:567–75.
[33] Raabe D, Lücke K. Mater Sci Technol 1993;9:302–12.
[34] Raabe D, Keichel J, Büscher M, Gottstein G. Proceedings of the 16th RISØ international symposium on materials science: materials: microstructural and crystallographic aspects of recrystallization. Roskilde, Denmark: RISØ National Laboratory; 1995. p. 517–23.
[35] Raabe D, Keichel J, Sun ZQ. J Mater Sci 1996;31:339–44.
[36] Konrad J, Zaefferer S, Schneider A. Mater Sci Forum 2004;467–470:75.
[37] Raabe D, Keichel J. Mater Sci Eng A 1995;203:208–16.
[38] Raabe D, Mao W. Philos Mag A 1995;71:805–13.
[39] Raabe D, Zhao Z, Park SJ, Roters F. Acta Mater 2002;50:421–40.
[40] Raabe D, Schlenkert G, Weisshaupt H, Lücke K. Mater Sci Technol 1994;10:229–305.
[41] Raabe D. Steel Res 1995;66:222–9.
[42] Humphreys FJ, Hatherly M. Recrystallization and related annealing phenomena. 2nd ed. Oxford, UK: Elsevier; 2004.
[43] Ferry M, Humphreys FJ. Acta Mater 1996;44:3089.
[44] Ferry M, Humphreys FJ, Johnson CP, Baggethun P. Proceedings of the ReX'96 3rd international conference on recrystallization and related phenomena. Monterey (CA): Monterey Institute of Advanced Studies; 1996. p. 323–30.
[45] Humphreys FJ, Ferry M, Paillard P, Johnson CP. Proceedings of the 16th international Risø symposium on materials science. Roskilde, Denmark: Risø; 1995. p. 87.
[46] Radhakrishnan B, Sarma G, Weiland H, Baggethun P. Model Simul Mater Sci Eng 2000;8:737–50.
[47] McKamey CG, Pierce DH. Scr Metall 1993;28:1173.
[48] Zaefferer S. La Revue de Métallurgie 2003;9:891.
[49] Stein F, Sauthoff G, Palm M. Z Metallkd 2004;95:469–85.
[50] Konrad J, Schneider A, Zaefferer S, Raabe D, Frommeyer G. Intermetallics 2005;13:1304–12.
[51] Zaefferer S, Konrad J, Raabe D. Microscopy conference 2005, Davos, Switzerland; 2005. p. 63.
[52] Kremer JR, Mastronarde DN, McIntosh JR. J Struct Biol 1996;116:71–6.
[53] Lipp S, Frey L, Lehrer C, Frank B, Demm E, Ryssel H. J Vac Sci Technol B 1996;14:3996–9.
[54] Ishitani T, Koike H, Yaguchi, Kamino T. J Vac Sci Technol B 1998;16:1907–13.
[55] Kato NI, Kohno Y, Saka H. J Vac Sci Technol A 1999;17:1201–4.
[56] Thomas I, Zaefferer S, Friedel F, Raabe D. Adv Eng Mater 2003;5:566–70.
[57] Hutchinson WB. Int Mater Rev 1984;29:25.
[58] Juntunen P, Raabe D, Karjalainen P, Kopio T, Bolle G. Metall Mater Trans A 2001;32:1989.
[59] Raabe D, Fischer-Bühner J, Ball J, Gottstein G. In: Liang Z, Zuo L, Chu Y, editors. Proceedings of the 11th international conference on textures of materials ICOTOM 11, vol. 2. Xi'an, China: International Academic Publishers; 1996. p. 941–50.